Disparity Estimation on Stereo Mammograms

Gautam S. Muralidhar, *Member, IEEE*, Alan C. Bovik, *Fellow, IEEE*, and Mia K. Markey, *Senior Member, IEEE*

***Abstract*— We consider the problem of depth estimation on digital stereo mammograms. Being able to elucidate 3D information from stereo mammograms is an important precursor to conducting 3D digital analysis of data from this promising new modality. The problem is generally much harder than the classic stereo matching problem on visible light images of the natural world, since nearly all of the 3D structural information of interest exists as complex network of multilayered, heavily occluded curvilinear structures. Toward addressing this difficult problem, we formulate a new stereo model that minimizes a global energy functional to densely estimate disparity on stereo mammogram images, by introducing a new singularity index as a constraint to obtain better estimates of disparity along critical curvilinear structures. Curvilinear structures, such as vasculature and spicules, are particularly salient structures in the breast, and being able to accurately position them in 3D is a valuable goal. Experiments on synthetic images with known ground truth and on real stereo mammograms highlight the advantages of the proposed stereo model over the canonical stereo model.**

***Index Terms*— Stereo mammography, stereo correspondence, disparity estimation, singularity index.**

I. Introduction

DIGITAL mammography remains the first choice modality for screening asymptomatic women for detecting signs of early breast cancer. Excellent image resolution (<100 microns per pixel) at a low radiation dose, reasonable cost, short image acquisition time, and ease of use have made mammography practical. However, mammography suffers from one major drawback: the loss of 3D information due to the projection of the breast onto a 2D image plane. The 3D to 2D projection process results in what is commonly referred to as anatomical noise due to overlapping out of plane tissue structures.

Anatomical noise is one of the key factors hindering the correct interpretation of a mammogram. For example, anatomical noise could obscure subtle cancers, or could cause false visual relationships between different tissue structures suggesting a cancer, where in reality there may exist none. Such inaccurate diagnoses often result in additional imaging tests and biopsy procedures that add to both monetary and emotional costs for women undergoing these procedures. Further, the positive predictive value of mammography in a routine screening program is quite low (10-30%) [1], [2]. These shortcomings have driven recent developments in the area of 3D breast imaging in the form of breast tomosynthesis [3], stereoscopic (stereo) mammography [4], and breast computed tomography (CT) [5]. Breast tomosynthesis has been recently approved by the Food and Drug Administration for clinical use in the U.S., while stereo mammography is currently undergoing clinical trials. Breast CT is still under investigation.

Stereo x-ray imaging and visualization of the breast provides the interpreting radiologist with a 3D view of the anatomical structures of the breast [4]. The advent of full field digital mammography, high quality digital displays, and stereoscopic devices have led to rapid progress in stereo mammography. In stereo mammography, two x-ray projection images of the breast are acquired at two slightly different angles. The angle of separation between the two x-ray images is typically between 4-10 degrees. The breast and the detector remain fixed in position while the x-ray source is rotating. The net radiation dose required for the stereo acquisition is kept equivalent to the dose required for digital mammography by distributing the dose between the two projections.

The resulting stereo mammogram is then viewed using a stereoscopic display and cross-polarized lenses. Stereo acute observers can fuse the stereo mammogram pair and perceive the structures throughout the breast in 3D. Stereo imaging contrasts with breast tomosynthesis and breast CT in which multiple projections are acquired over a much wider angular range (15-50 degrees for tomosynthesis and 360 degrees for breast CT). However, as demonstrated in [6]–[8], it is possible to view tomosynthesis projection images using a stereoscopic display. Stereo imaging and visualization of the breast has already shown great promise in improving upon the specificity of breast cancer detection and reducing unnecessary patient recalls, while at the same time not compromising on the sensitivity of breast cancer detection, as demonstrated by the clinical studies of Getty *et al.* [4] and D'Orsi *et al.* [9].

The advent of stereo mammographic imaging, while still nascent, has opened the door for the development of computational tools for visualizing and interpreting stereo mammograms. At the crux of computational stereo lies the stereo correspondence or matching problem. Stereo matching is the process of matching each pixel in one of the stereo views to candidate pixels in the other view. Finding the best match yields a positional difference known as disparity arising from the slightly different geometries of the captured views.

Manuscript received July 12, 2013; revised May 2, 2014, August 28, 2014, and January 7, 2015; accepted May 8, 2015. Date of publication May 13, 2015; date of current version June 2, 2015. The associate editor coordinating the review of this manuscript and approving it for publication was Prof. Rebecca Willett.

G. S. Muralidhar is with Pivotal Software, Inc., Palo Alto, CA 94304 USA (e-mail: gautam.sm@utexas.edu).

A. C. Bovik is with the Department of Electrical and Computer Engineering, The University of Texas at Austin, Austin, TX 78712 USA (e-mail: bovik@ece.utexas.edu).

M. K. Markey is with the Department of Biomedical Engineering, The University of Texas at Austin, Austin, TX 78712 USA (e-mail: mia.markey@utexas.edu).

Color versions of one or more of the figures in this paper are available online at http://ieeexplore.ieee.org.

Digital Object Identifier 10.1109/TIP.2015.2432714

Once the disparity is estimated at a sufficient number of image locations in the reference view, it is possible to reconstruct the geometry of the original 3D scene using knowledge of the imaging geometry. However, estimating the optimal disparity given just the two views of the stereo pair is an ill-posed problem. A pixel in the reference view could have multiple candidate matches (often known as the problem of non-uniqueness) in a 2D search window in the other matching view. The size of this search window is not known *a priori*.

To simplify the matching process, the epipolar assumption is often made use of. The epipolar assumption constrains the candidate matches to lie along a specific line or a curve in the 2D plane, which can be determined with the knowledge of the imaging geometry, thereby simplifying the search problem to a 1D problem. For convenience, it is often assumed that the epipolar lines correspond to the image rows, which have been aligned to correspond to one another in each of the two views. This assumption can be asserted under a non-vergent parallel baseline imaging geometry, but only holds approximately for a vergent imaging geometry provided the angle of separation between the views is small (typically less than 12-15 degrees). However, even with the epipolar constraint in place (irrespective of whether they are based on the imaging geometry or not), the disparity estimation problem is still complicated by factors such as non-uniqueness of intensity matches (along a 1D search window), half occlusions (points of the 3D scene seen only in one image and not in the other), and transparency (seeing through objects). These kinds of phenomena occur throughout typical stereo mammogram images.

The focus of this paper is a novel computational stereo model that is specifically directed towards estimating a dense disparity map from a pair of stereo mammograms. As demonstrated in prior observer studies with stereo mammography ([6]–[8]), radiologists can perceive depth throughout the breast. This suggests that there is enough opacity contained in various structures of the breast such as parenchymal tissue, masses, and curvilinear structures, thereby necessitating dense disparity estimation algorithms. The problem of reliably estimating a dense disparity map from a pair of stereo mammogram images is very important since this is the first step towards developing computational tools for interpreting stereo mammograms. These tools will assist the radiologist in interpreting stereo mammograms when the modality is routinely used in the clinical workflow. Example usage of computational tools for stereo mammogram interpretation include quantifying parenchymal patterns and breast density in 3D, measuring lesion properties in 3D, and estimating the depth at which a tumor is located, providing highly localized 3D information for lesion biopsy.

A peculiarity of mammograms is the presence of many singularities in the form of curvilinear structures of various lengths, widths, and tortuosities, which exhibit a complex occlusion pattern. This is unlike what is seen in optical images of typical natural scenes, which are largely comprised of piece-wise smooth surfaces. Computational stereo algorithms for natural scenes exploit this property and constrain the resulting disparity to be piece-wise smooth. In the case of stereo mammograms, piece-wise smoothness is violated at singular points often arising out of a network of curvilinear structures comprised of vasculature, ducts, lobules and spicules. For example, Fig. 1 illustrates a pair of stereo mammogram images. Stereo acute observers can fuse this pair without using any stereoscopic devices by just crossing their eyes. The resulting 3D view in the brain, also known as the cyclopean view, is comprised of a number of curvilinear structures lying in different depth planes. Preserving these curvilinear structures in the disparity space is important in order to estimate the depth at which these structures lie. Indeed, the reliable detection of curvilinear structures in mammograms has been a widely studied problem and continues to be of interest for developing robust computer-aided detection (CADe) and diagnosis (CADx) algorithms (see [10], [11]). Towards solving this difficult aspect of the problem, our proposed model employs a novel singularity index that was recently developed to reliably detect singular points in images [12], [13]. The singularity index can be configured to detect point mass like structures such as impulses in a 1D signal or curvilinear masses in images, while rejecting step edges. It can also be configured to do the opposite. Experimental results on synthetic images with known ground truth data and on real stereo mammograms show the advantages of the proposed model over the canonical model for our application.

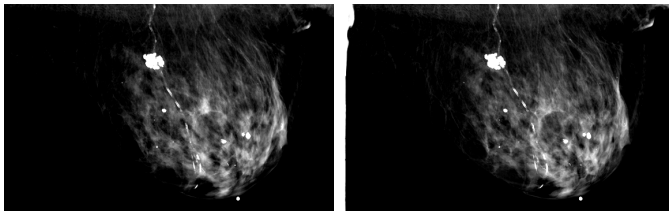

Fig. 1. A pair of stereo mammogram images.

The rest of the paper is organized as follows: We begin with a short review of existing work in computational stereo for natural scenes and mammographic images in Section I. A. In Section II, we describe the baseline stereo models, which serves as comparisons for the proposed model. Section III discusses the proposed stereo model, while Section IV provides details on the optimization strategy. We describe the experimental methodology and results in Sections V and VI, respectively. We conclude with a brief discussion in Section VII.

A. Relevant Work on Disparity Estimation

There exists a large body of work on computational stereo for disparity estimation. A detailed review of computational stereo is provided in [14] and [15]. Broadly speaking, existing disparity estimation algorithms are founded on the premise of brightness (or color) constancy, i.e., the projected brightness (or color) of 3D scene points visible on both the stereo views are similar. The brightness constancy assumption is often handled via a matching/similarity cost function that assigns a cost based on the projected brightness values at the corresponding points of the two views. It should be noted

that other matching cost functions such as those based on luminance derivatives and mutual information have been explored to handle images having radiometric differences resulting in unequal projected brightness values [16]. However, brightness constancy alone is insufficient to reliably estimate the disparity due to problems associated with non-uniqueness and half occlusions as described before. As a result, the brightness constancy assumption is often augmented with a disparity smoothness assumption, which penalizes large changes in the disparity gradient. The disparity smoothness assumption is based on the premise that natural 3D scenes are composed of objects and surfaces that are largely piecewise smooth. With these assumptions in place, stereo algorithms fall under two broad categories: 1) local algorithms, and 2) global algorithms.

Local algorithms are typically window-based, where the best matching disparity at a given pixel is dependent on the intensity (or color) values within a local window [14]. The disparity smoothness assumption is typically enforced by aggregating support from neighboring pixels within the local window. Global algorithms pose the disparity estimation problem as an optimization problem [14], where in an energy functional containing a brightness constancy term, or photometric constraint, and the disparity smoothness term is minimized using an optimization algorithm such as simulated annealing [17], graph cuts [18], or variational level sets [19].

Disparity estimation algorithms are sometimes also categorized as sparse or dense algorithms [14]. Sparse algorithms typically employ a feature detector such as an edge or a curvilinear structure detector on the reference image and estimate disparity only at points of high confidence feature extraction. The motivation behind sparse algorithms is to eliminate matching in textureless regions where disparity estimation is often compounded by non-unique matches. Dense stereo algorithms attempt to estimate disparity at every point of the reference image. Disparity estimation algorithms could also be either single scale or multi-scale. Single-scale algorithms operate only on the original image resolution, while multi-scale algorithms (see [17], [19]) employ a hierarchical coarse-to-fine approach, where the disparity estimated at a coarser scale is supplied as an initial estimate to the disparity estimation process at the subsequent finer scale. Low-pass and band-pass image pyramids [20] are commonly employed in multi-scale stereo algorithms. The Middlebury website [21] contains a comprehensive evaluation of various kinds of stereo algorithms on benchmark natural scene data sets.

Computational stereo and disparity estimation has also been studied for applications involving microscopic and medical images. For instance, Kim *et al.* [22] presented one of the earlier algorithms concerning the estimation of disparity in stereo images of biological specimens obtained from a stereo light microscope. Theirs was a sparse algorithm that estimated disparity at points of high gradient magnitude and subsequently recovered the 3D shapes of contours evident on vascular cast stereo images. One of the first algorithms for stereo mammography was proposed by Chelberg *et al.* [23]. They used Laplacian of Gaussian (LOG) filters for performing stereo matching on a stereo mammography pair of a digital phantom. Corresponding points were matched only between zero-crossings of the same sign and roughly the same orientation in the left and right images, thereby resulting in sparse disparity estimates. Other research groups have proposed algorithms for extracting corresponding features from two-view stereo-axial biopsy mammograms and standard two-view (MLO and CC) mammograms for use in computer-aided diagnosis of breast cancer (see [24], [25]). However, this is a much harder problem since the two views are acquired over a very wide angle (between 30-60 degrees) with different amounts of compression.

II. Baseline Stereo Models

We first describe the canonical stereo model, one of the baselines for comparing the performance of the proposed stereo model. Let $I_1(\mathbf{x})$ and $I_2(\mathbf{x})$ denote the two images of a rectified stereo pair (such that the corresponding rows are registered), where $\mathbf{x} = (x, y)^T$ represents an image pixel location belonging to the discrete rectangular domain Z^2. Let $I_1(\mathbf{x})$ denote the reference image. Let $D(\mathbf{x})$ denote the integer-valued disparity at the image location $\mathbf{x}$. Then, according to the canonical stereo model, D is computed as the minimizer of the following energy functional:

$$E(D(\mathbf{x})) = E_P(D(\mathbf{x})) + \lambda_1 E_S(D(\mathbf{x})), \tag{1}$$

where $E_P(D(\mathbf{x}))$ represents the photometric term, $E_S(D(\mathbf{x}))$ represents the disparity smoothness term, and λ_1 is a weight indicating the relative importance of the smoothness term.

The photometric term penalizes disparity assignments that result in large intensity differences between the corresponding points: $E_P(D(\mathbf{x})) = (I_1(x, y) - I_2(x + D(x, y), y))^2$. By penalizing large intensity differences between the corresponding points of a stereo mammogram pair, we implicitly assume that the projected intensities along two linear x-ray trajectories separated by a small angle are similar. The disparity smoothness term penalizes large changes in disparity gradient and is defined as the sum of absolute difference in disparity between that assigned to a given pixel and its immediate neighbors: $E_S(D(\mathbf{x})) = \sum_{\mathbf{p} \in N} |D(\mathbf{x}) - D(\mathbf{p})|$, where $\mathbf{p}$ is a pixel location in the neighborhood N of $\mathbf{x}$.

The canonical model is optimized using simulated annealing. There are a number of stereo matching optimization algorithms available [14], but not all are suitable for the problem on hand. As described in [18], the optimization strategy used to minimize a stereo functional plays a crucial role in obtaining favorable disparity results, even if the model is the simple canonical model described here. However, in comparing functional models of binocular matching and task-specific features underlying these models, it is important to deploy equivalent optimization strategies when making the comparisons. Therefore we utilize simulated annealing as the baseline optimization method to test the compared models. Thus we compare the models directly by adopting the same optimization strategy. While the canonical stereo model can be optimized using graph cuts [18], which we also illustrate in this paper, this approach is not feasible for the stereo

mammographic model described in section III due to the presence of complex, non-linear second order regularizers in the objective function.

As a second baseline stereo model, we use a top-performing objective function in the Middlebury stereo evaluation [21], originally put forth by Woodford *et al.* [26] for comparing the performance of the proposed stereo model. The stereo model proposed in [26] employs a second order smoothness prior for the regularizer term $E_S(D(\mathbf{x}))$ and is defined as $E_S(D(\mathbf{x})) = \sum_{\mathbf{p},\mathbf{q}\in N} W(N)|D(\mathbf{p}) - 2D(\mathbf{x}) + D(\mathbf{q})|$, where $\mathbf{p}$ and $\mathbf{q}$ are pixel locations in the neighborhood N of $\mathbf{x}$ and $W(N)$ describes a weighting term associated with the pixels in the neighborhood N. The second order smoothness prior approximates the second derivative of the disparity function. The neighborhood N is defined over the set of all 3×1 and 1×3 patches, which are centered at the current pixel location $\mathbf{x}$. The weighting term $W(N)$ is set to encourage disparity edges to coincide with the edges in the reference image. Woodford *et al.* [26] argue in favor of second order smoothness priors over the first order smoothness priors such as those defined in the canonical stereo model since the first order smoothness prior encourages low curvature fronto-parallel planes, which is rarely the case in real world stereo images and in stereo mammograms. While the objective function is optimized using an extension of the "QPBO" algorithm in the original work [26], here we optimize it using simulated annealing for the same reasons described in the canonical stereo model baseline comparison.

III. Proposed Stereo Model

A drawback of the two baseline stereo models is that neither model is designed to promote curvilinear masses in disparity space to better preserve fine-scale curvilinear structures. The model by Woodford *et al.* [26] disables the second order smoothness term at edge locations of the reference image, but does not explicitly promote curvilinear masses in disparity space. We build on this strategy of disabling the smoothness terms at the edge locations of the reference image, but further refine it to handle both depth discontinuities arising from edges, and from complex patterns of impulse-like occluding fine scale curvilinear structures that need to be preserved in the disparity space. The problem of preserving depth discontinuities and promoting curvilinear masses in disparity space necessitates the reliable detection of singularity locations in the reference view of the stereo mammogram pair.

Two kinds of singularities are encountered in stereo mammograms: a) impulse singularities, such as those arising from isolated curvilinear masses or the medial axis of fine scale curvilinear structures, and b) edge singularities, such as those arising from the boundaries of curvilinear structures and other anatomical components. Fig. 2 shows one view of two different stereo mammograms (top) with multiple scan-lines highlighted in color. Also shown in Fig. 2 (bottom) are the corresponding 1D cross-sectional luminance profiles along the different scan-lines. The presence of impulse and edge singularities is clearly evident in the 1D luminance cross-sectional profiles (Fig. 2 (bottom)). Towards finding these kinds of singularities reliably and robustly in images, we have recently developed a new singularity index [12], [13]. We briefly review this next.

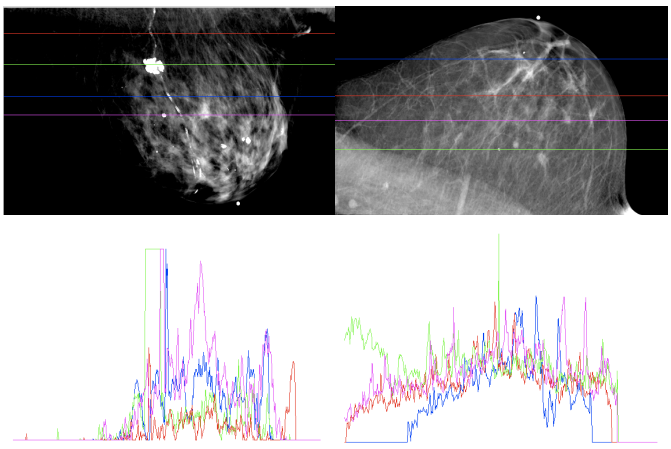

Fig. 2. One view of two different stereo mammogram pairs (top) with multiple scan-lines highlighted in color. The corresponding 1D luminance cross sectional profiles are shown in the bottom.

A. A New Singularity Index

Since our model operates on a raster basis, we introduce the singularity index in 1D although it can be defined on functions of arbitrary dimensionality [12]. Let $f(x), x \in R$ be a 1D function, where for example, $f(x)$ could represent the 1D luminance cross-sectional profiles shown in Fig. 2 (bottom). Also, let $f'(x)$ and $f''(x)$ denote its first and second order derivatives, respectively. The singularity index is then defined as the dimensionless ratio:

$$\psi[f(x)] = \frac{|f(x)f''(x)|}{1 + |f'(x)|^2} \tag{2}$$

Invariance to underlying local brightness offsets is ensured by locally debiasing the function $f(x)$ by everywhere subtracting the local mean computed using a large, unit area gaussian filter (g_λ). The scale λ of this gaussian filter may be chosen as a function of the scale and fractional magnitude of the signal to be detected, which we model as an isolated smoothed point mass of height K and scale w: $f(x) = Ke^{\frac{-x^2}{2w^2}}$. A good criterion to ensure large response is to force $|f(0) - \hat{f}(0)| \leq \epsilon K$, where $\hat{f}(x) = f(x) - g_\lambda(x) * f(x)$ is the locally debiased signal and $\epsilon \in (0, 1]$ yields the lower bound $\lambda \geq w\sqrt{\frac{1-\epsilon^2}{\epsilon^2}}$.

According to this design, the 1D cross-sectional profiles of isolated curvilinear masses, whose twice derivative is large and once derivative is small will yield a strong response to the index ψ, while edge singularities, as might arise from structures other than curvilinear masses, whose once derivative is large and twice derivative is small will yield a desirable weak response to the index. Thus, the singularity index is highly specific to and sensitive to important breast structures. This can be seen by modeling the 1D cross-sectional profile of a thin curvilinear structure as a gaussian of height $K > 0$ and scale w: $f(x) = Ke^{\frac{-x^2}{2w^2}}$, for which the index evaluates to

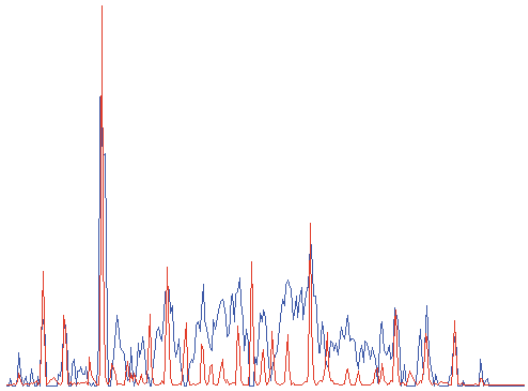

Fig. 3. Response of the smoothed singularity impulse index (red) when applied to a 1D luminance cross-sectional profile from a stereo mammogram image (blue).

$\left|\frac{K^2}{w^2}\right|$ at the origin. As K increases, or as w decreases, $\psi[f(0)]$ also increases, as desired. Conversely, for an input that is a smoothed edge: $f(x) = Ke^{\frac{-x^2}{2w^2}} * u(x)$, where $u(x)$ is the unit-step, the index evaluates to 0 at the origin.

The scale of the singularity index can be controlled by introducing pre-filtering, creating a 'smoothed index':

$$\psi_\sigma[f(x)] = \frac{|g_\sigma * f(x)||g''_\sigma * f(x)|}{1 + |g'_{\alpha\sigma} * f(x)|^2}, \tag{3}$$

where, g is a smoothing filter such as an unit-area gaussian: $g_\sigma(x) = \frac{1}{\sqrt{2\pi}\sigma} e^{\frac{-x^2}{2\sigma^2}}$. The use of gaussian filters to smooth the signal stabilizes derivative computations and reduces the effect of noise. The factor α allows for an optimized impulse against edge-side lobe response (see [13]). We use the value $\alpha = 1.7754$ based on arguments given in [13]. The smoothed singularity index (3) can be easily extended to detect impulses at any or multiple scales by using the scale normalized index $\psi_{\sigma,norm}[f(x)] = \sigma^2\psi_\sigma[f(x)]$. The response of the smoothed singularity index (3) when applied to a 1D luminance cross-sectional profile from a stereo mammogram image is illustrated in Fig. 3. It is evident from Fig. 3 that the singularity index responds strongly to isolated impulses and is not sensitive to the polarity of the impulse.

The smoothed singularity index (3) can also be generalized to detect other types of singularities such as edges, which may arise from important breast structures such as large masses and dense (radio-opaque) tissues. Consider the k^{th}-order index

$$\psi^k_\sigma[f(x)] = \frac{|g^{k-1}_\sigma * f(x)||g^{k+1}_\sigma * f(x)|}{1 + |g^k_{\alpha\sigma} * f(x)|^2}, \tag{4}$$

where $(k = 1)$ yields (3), an impulse index. Likewise, $k = 2$ yields an edge singularity index that responds strongly to edges, while responding minimally to impulses.

The singularity index is extended to 2D by adopting a design mechanism inspired by Canny for edge detection [27]. We first determine the direction $\theta(x, y)$ at each pixel along which the second derivative of the gaussian smoothed image attains a local extremum, which is a good estimate of the direction orthogonal to the singularity. Once this direction is estimated, we evaluate the responses of the gaussian derivative filters along this direction and compute the singularity index. The steerable property of the derivatives of an isotropic gaussian enable the various derivative responses to be computed efficiently as described in [28]. Non-maxima suppression (NMS) is finally applied to the index response along the dominant orientation $\theta(x, y)$.

Note that the simple second derivative operator can be used to detect impulse singularities. However, a detailed theoretical analyses described in [29] reveals that the singularity index has better robustness to noise and yields a much smaller side lobe response to edges than does the second derivative operator. The results of these analyses [29] motivate the use of the new singularity index in the current application in which the disparity space is partitioned into piece-wise smooth regions, edges, and curvilinear structures. For the approach to succeed, the operator response to edges and curvilinear structures needs to be mutually exclusive, and the new singularity index has this property.

B. Singularity Index for Disparity Estimation

We employ both the impulse and edge singularity indices to specifically enhance the difficult disparity estimation of critical curvilinear structures such as spicules and vasculature seen on a pair of stereo mammogram images. Their purpose is two-fold: 1) the 2D impulse and edge singularity indices applied to the reference view of a stereo mammogram pair provide valuable cues to the locations where the disparity smoothness constraint needs to be de-emphasized, and 2) the 1D impulse index is used to promote curvilinear masses at locations where the 2D impulse index produced a strong response when applied to the reference view of the stereo mammogram pair. The complete stereo model is defined as follows:

$$\begin{aligned} E(D(\mathbf{x})) = {} & E_P(D(\mathbf{x})) \\ & + (1 - w_1(\mathbf{x}))(1 - w_2(\mathbf{x}))E_S(D(\mathbf{x})) \\ & + w_2(\mathbf{x})E_C(D(\mathbf{x})), \end{aligned} \tag{5}$$

where the term $E_P(D(\mathbf{x}))$ enforces the photometric constraint and is defined as in the well-known canonical stereo model, the term $E_S(D(\mathbf{x}))$ enforces the disparity smoothness constraint, and the term $E_C(D(\mathbf{x}))$ promotes curvilinear masses in disparity space. Further, $w_1(\mathbf{x})$ and $w_2(\mathbf{x})$ serve to control $E_S(D(\mathbf{x}))$ and $E_C(D(\mathbf{x}))$, and are defined as functions of the edge index (ψ^2_σ) and the impulse index (ψ^1_σ) applied to the reference image, respectively: $w_1(\mathbf{x}) = 1 - L(\psi^2_\sigma[I_1(\mathbf{x})])$ and $w_2(\mathbf{x}) = 1 - L(\psi^1_\sigma[I_1(\mathbf{x})])$. The function $L(v) = exp(-\frac{v}{C_T})$ maps the singularity index response to the range [0, 1], where the constant $C_T \in R$ is a threshold on the index value. $w_1(\mathbf{x}) \to 1$ implies the presence of an edge at the location $\mathbf{x}$ in the reference image, while $w_2(\mathbf{x}) \to 1$ implies the presence of an impulse at the location $\mathbf{x}$.

The disparity smoothness term is defined as $E_S(D(\mathbf{x})) = \lambda_1 \sum_{\mathbf{p}\in N}(1 - w_1(\mathbf{p}))|D(\mathbf{x}) - D(\mathbf{p})|$, where $\mathbf{p}$ is a pixel location in the neighborhood N of $\mathbf{x}$, and λ_1 is a weight indicating the relative importance of the term. The smoothness term E_S ceases to apply between pairs of neighboring pixels when

either pixel is an edge pixel, i.e. $w_1 \rightarrow 1$ at either pixel. Likewise, curvilinear masses are promoted via the term E_C in disparity space at locations where $w_2(\mathbf{x}) \rightarrow 1$. We next describe the term E_C in detail.

C. Promoting Curvilinear Masses

We hypothesize that critical, fine-scale curvilinear masses such as vasculature and spicules that are contained in the breast are characterized by large second derivatives and small first derivatives in the direction orthogonal to the axes of the curvilinear masses in disparity space. On the other hand, it has been perviously shown [30] that disparity varies smoothly along image contours projected from 3D contours. The term E_C embodies both these properties of curvilinear masses and is defined as follows:

$$\begin{aligned} E_C(D(\mathbf{x})) = \lambda_2\{&(|D(\mathbf{q}) - D(\mathbf{x})| + |D(\mathbf{x}) - D(\mathbf{p})|) \\ &+ (|D(\mathbf{q}) - 2 * D(\mathbf{x}) + D(\mathbf{p})|)\} \\ &- \lambda_3(\sigma^2 \psi_\sigma[D(\mathbf{x})]), \end{aligned} \tag{6}$$

where $\mathbf{p}$ and $\mathbf{q}$ are locations in a 3×3 neighborhood of $\mathbf{x}$, and λ_2 and λ_3 represent the relative weights of the individual terms.

We employ the 1D scale-normalized smoothed singularity index (3) in (6) to promote large second derivatives and small first derivatives in the direction orthogonal to a curvilinear mass in disparity space. Since (6) is applied point-wise at locations of isolated impulses and curvilinear masses estimated by the weighting function w_2 from the reference image of the stereo pair (*i.e.* the location of the impulses are pre-computed), the factor α in (3) is set to 1. Further, the convolution operator in (3) is replaced by the simple inner product.

The first two terms in (6) augment the singularity index by ensuring that disparity varies smoothly and continuously along the axes of curvilinear masses [30]. Hence, neighboring locations $\mathbf{p}$ and $\mathbf{q}$ are selected to lie along the curvilinear mass, i.e. along a direction orthogonal to the dominant orientation $\theta(\mathbf{x})$, whose estimate is obtained from the 2D singularity index applied to the reference image of the stereo pair (here we define the dominant orientation to be the orientation that is along the unit normal vector to a point on the curvilinear structure)). In (6), the singularity index ψ_σ is applied to a 1D sequence of disparity values in a neighborhood of $\mathbf{x}$ defined along the dominant orientation. The size of this neighborhood is dependent on the scale σ of the 1D gaussian filter in (3). The dominant orientation θ at each pixel location $\mathbf{x}$ is quantized to lie along one of four directions (east-west, northeast-southwest, north-south, northwest-southeast) surrounding the pixel location $\mathbf{x}$. The locations $\mathbf{p}$ and $\mathbf{q}$ are then chosen to be along a direction orthogonal to the dominant orientation (i.e. along the unit tangent vector to a point on the curvilinear structure). This is illustrated in Fig. 4.

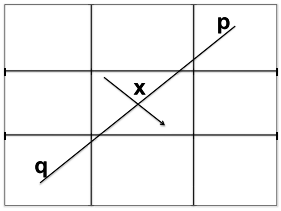

Fig. 4. The dominant orientation of a curvilinear structure at location $\mathbf{x}$ is illustrated by the arrow. The locations $\mathbf{p}$ and $\mathbf{q}$ are the neighboring locations orthogonal to the dominant orientation.

IV. Multi Scale Optimization

We employ the Metropolis simulated annealing algorithm to optimize both the proposed stereo model (5) and the canonical stereo model (1). While slow, the Metropolis simulated annealing algorithm has been shown to produce good disparity estimates provided the annealing schedule is properly selected [17]. We adopt a hierarchical, coarse-to-fine multi-scale optimization approach that iteratively smooths and sub-samples the stereo images by a factor of two. Simulated annealing is run at each scale and the disparity obtained from a coarser scale serves as the initialization at the subsequent finer scale. The disparity estimated at a coarser scale is linearly interpolated and multiplied by a factor of 2 prior to using it as an initial estimate at each subsequent finer scale. Algorithm 1 gives the pseudo-code for the optimization of the proposed model at a given hierarchical scale.

Algorithm 1 Optimization of the Proposed Stereo Model

Inputs: Stereo image pair I_1 and I_2 with I_1 taken as the reference image, an initial estimate for the disparity map D, and the weighting functions w_1 and w_2 computed by applying the 2-D singularity index ψ_σ on I_1.

Output: The final disparity map D for I_1.

```
Set a start temperature T.
while T > end temperature do
  for each pixel location x in I_1 do
    D_1 ← D(x)
    Compute E(D_1) = E_P(D_1) + (1 − w_1(x))(1 − w_2(x))E_S(D_1) + w_2(x)E_C(D_1).
    Sample a new disparity D_2 uniformly from the range [D_L, D_U].
    Compute E(D_2) = E_P(D_2) + (1 − w_1(x))(1 − w_2(x))E_S(D_2) + w_2(x)E_C(D_2).
    ΔE ← E(D_2) − E(D_1)
    if ΔE < 0 then
      D(x) ← D_2
    else
      Select a random number r uniformly from the range [0, 1].
      if r ≤ exp(−ΔE/T) then
        D(x) ← D_2
      end if
    end if
  end for
  T ← T − ΔT
end while
```

V. Experimental Methodology

A. Creation of Synthetic Mammograms

Real stereo mammogram images lack ground truth disparity data. Hence, only qualitative results of the proposed

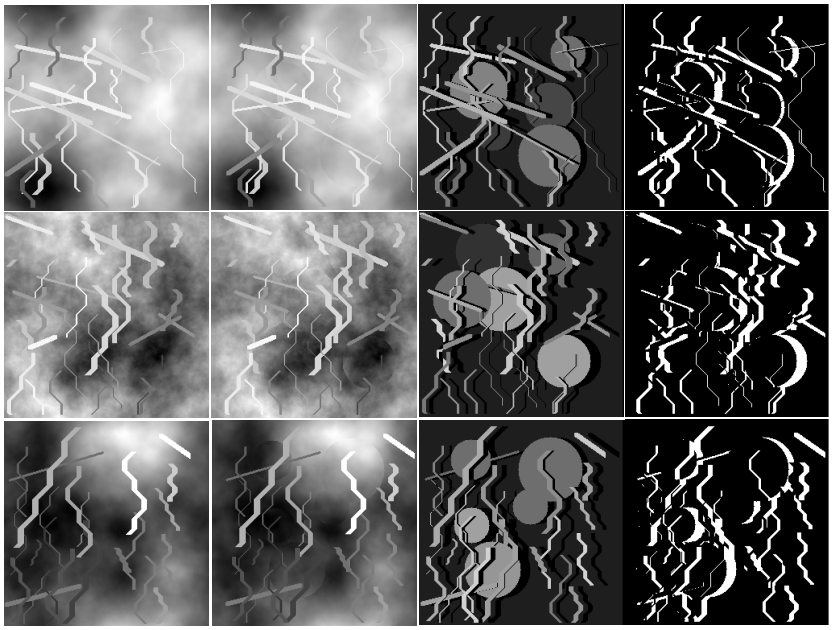

Fig. 5. Examples of synthetic stereo images. The reference image is shown in column 1, while the ground truth disparity and the ground truth occlusion maps are shown in columns 3 and 4, respectively. Occluded pixels in the ground truth disparity map have 0 intensity.

and canonical stereo models can be shown on real stereo mammograms. In order to quantitatively compare the proposed and canonical stereo models, 50 synthetic stereo images with ground truth disparity data were generated. The synthetic images were created with an $1/f^{\beta}$ background texture. For each stereo pair, the exponent β was a random number uniformly generated on $[1.0, 2.5]$ to resemble mammographic texture [31]. The background texture was assigned a global disparity of 3 pixels.

Five circular regions whose centers and radii were randomly selected in the reference image were horizontally displaced by a random disparity value uniformly selected from the range 5-16 pixels in the other image of the stereo pair. Each center coordinate was constrained to lie within the image plane and to be the only coordinate within a 25×25 window around it. The radii of the circular regions were uniformly selected from the range 20-40 pixels.

Curvilinear structures were then overlaid on the background texture in the reference image. The intensity along the curvilinear structures was set to a constant whose value was computed as the sum of the background intensity at the first coordinate of the curvilinear structure and a random positive offset. The number, orientation, starting coordinate, length, width, and the disparity of the curvilinear structures in each stereo pair were randomly selected. The number of curvilinear structures was uniformly generated on $[20, 30]$, each starting coordinate was constrained to lie within the image plane and to be the only coordinate within a 25×25 window around it, while the length, width, and disparity of each curvilinear structure was uniformly selected from 30-150 pixels, 1-8 pixels, and 11-21 pixels, respectively.

Each curvilinear structure was created as follows: a random number was uniformly generated on $[0, 1]$. If the value of this random number was greater than 0.75, then the curvilinear structure was created as a straight line between two end points using the Bresenham line algorithm [32]. Given the start coordinate, the end coordinate was determined based on the length and orientation of the straight line. The orientation was a random number uniformly selected from 5-30 degrees. If the random number was less than 0.75, the curvilinear structures

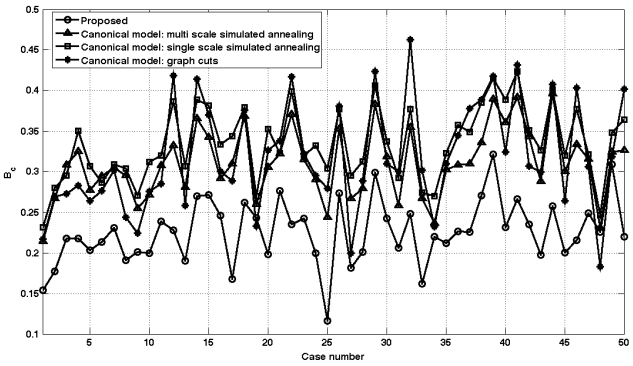

Fig. 6. Percent bad pixel error of the proposed and the canonical single-scale and multi-scale stereo models along the curvilinear structures.

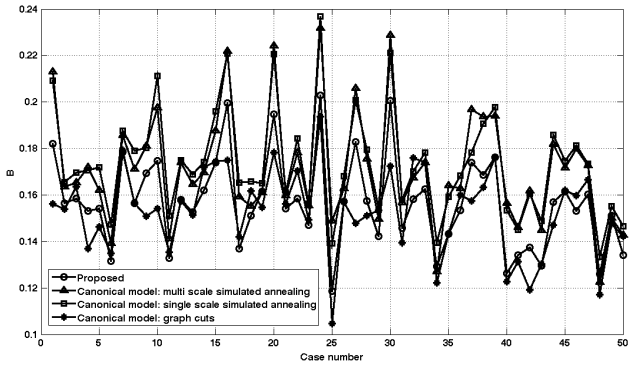

Fig. 7. Overall percent bad pixel error of the proposed and the canonical single-scale and multi-scale stereo models.

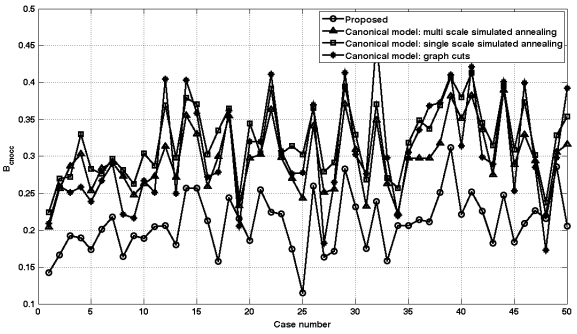

Fig. 8. Percent bad pixel error of the proposed and the canonical single-scale and multi-scale stereo models along the non-occluded curvilinear pixels.

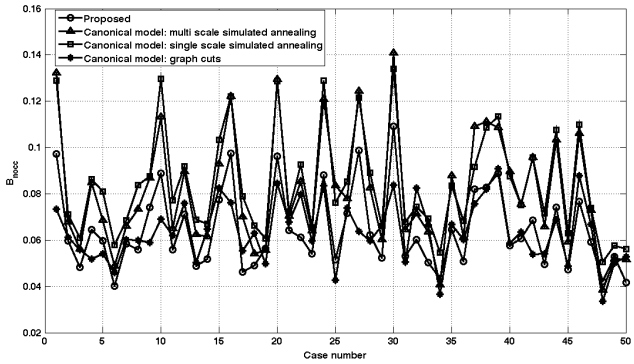

Fig. 9. Overall percent bad pixel error of the proposed and the canonical single-scale and multi-scale stereo models for only the non-occluded pixels.

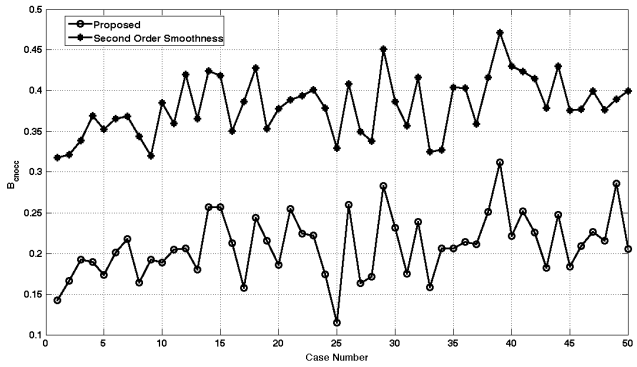

Fig. 10. Percent bad pixel error of the proposed and the second order smoothness stereo models along the non-occluded curvilinear structures.

were generated using a contour traversal algorithm with tortuousity. First, given the start coordinate, a direction of growth was randomly selected. This could either be south (vertical), southeast (diagonal right), or southwest (diagonal left). After traversing in this direction for $1/9^{th}$ of the length, the direction of traversal was changed. If the previous direction of traversal was either southeast or southwest, then the new direction of traversal could only be south, while if the previous direction was south, then the new direction was randomly selected to be either southeast or southwest. The traversal continued till the pre-specified length of the contour was reached or the contour grew out of the image plane. Fig. 5 illustrates three examples of synthetic stereo images with ground truth disparity data and occlusion maps created in this way. Though these synthetic images provide a gross resemblance of the

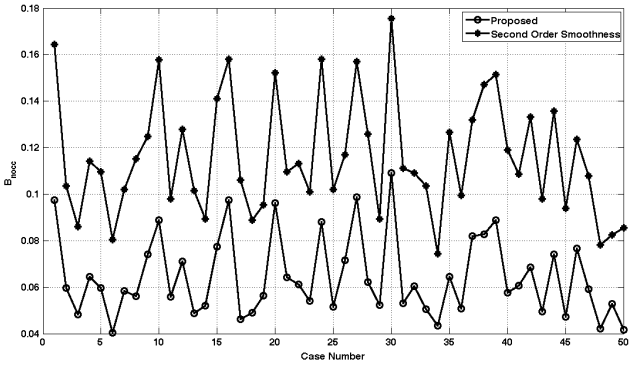

Fig. 11. Overall percent bad pixel error of the proposed and the second order smoothness stereo models for only the non-occluded pixels.

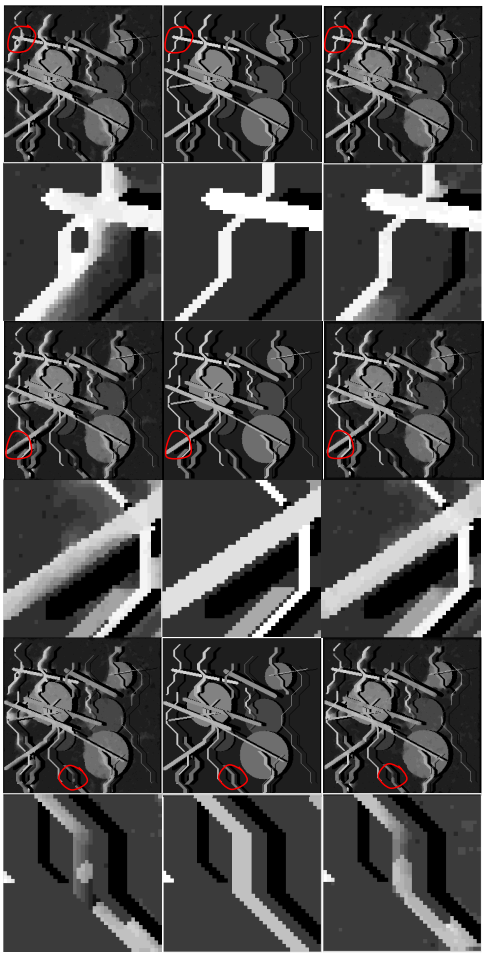

Fig. 12. Results of the proposed and the multi-scale canonical stereo models (simulated annealing) on the synthetic stereo pair illustrated in row 1 in Fig. 5. Column 1: disparity estimated from the canonical model, Column 2: ground truth disparity, and Column 3: disparity estimated from the proposed model. Three different regions outlined in red in rows 1, 3, and 5 are shown up close in rows 2, 4, and 6 to illustrate examples of regions were the disparity estimates produced by the canonical model were incorrect.

structures present in a real mammogram, they represent the first dataset of their kind and provide valuable ground truth disparity.

B. Parameter Setting

Here, we describe the parameter settings that are used in the baseline and proposed stereo models. The parameter λ_1, which

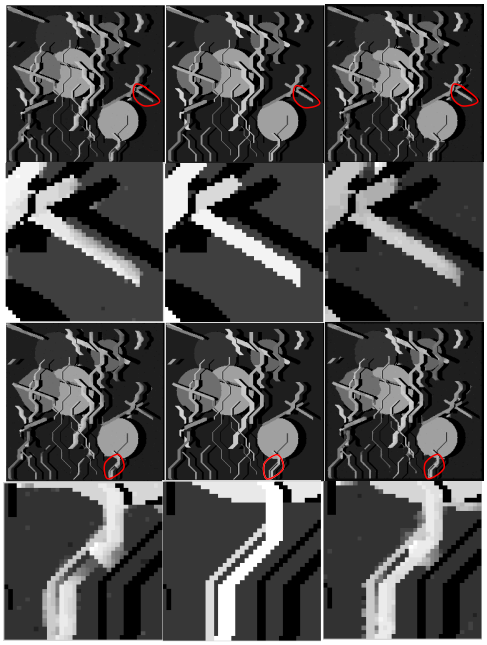

Fig. 13. Results of the proposed and the multi-scale canonical stereo models (simulated annealing) on the synthetic stereo pair illustrated in row 2 in Fig. 5. Column 1: disparity estimated from the canonical model, Column 2: ground truth disparity, and Column 3: disparity estimated from the proposed model. Two different regions outlined in red in rows 1 and 3 are shown up close in rows 2 and 4 to illustrate examples of regions were the disparity estimates produced by the canonical model were incorrect.

controls the disparity smoothness constraint is common to both the models. Typically, λ_1 is set according to the application. For example, if the 3D scene is composed of primarily piece-wise smooth surfaces, then λ_1 is set to a large value to enforce the disparity smoothness constraint tightly. On the other hand, in the stereo-mammography application, the breast is composed of very few piece-wise smooth surfaces, that usually arise from solid breast masses and dense (radio-opaque) tissues. Hence, we set $\lambda_1 = 1$ in both the models. If λ_1 is set to a large value, then the resulting disparity space will be over-smoothed. We used an 8-connected square neighborhood ($N = 8$) to evaluate the smoothness constraint.

The parameters λ_2 and λ_3 are specific to the proposed model and control the continuity and promotion of curvilinear masses in disparity space, respectively. We set $\lambda_2 > \lambda_3$, thereby placing a stronger emphasis on disparity continuity along the direction of curvilinear masses. We set $\lambda_2 = 100$ and $\lambda_3 = 5$. These parameters were found to yield good performance on the synthetic stereo pairs. Note that one could also adopt the more computationally intensive grid-search and cross-validation processes [33] to arrive at values for the parameters λ_2 and λ_3.

The number of hierarchical scales used in the multi-scale optimization process was set to 3. At each hierarchical scale of optimization, both the 2D impulse and edge singularity indices were applied to the reference view of the stereo pair at that scale. The 2D impulse index was applied to detect fine scale curvilinear structures at each hierarchical scale of optimization, and hence we set $\sigma = 1.5$ pixels. Similarly, the scale σ of the 1D impulse index that is used to promote curvilinear masses in disparity space in (6) was set

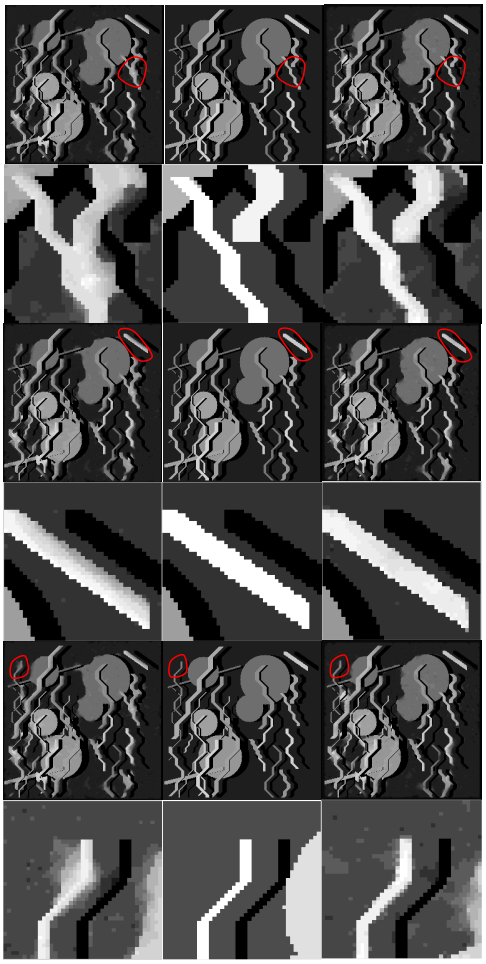

Fig. 14. Results of the proposed and the multi-scale canonical stereo models (simulated annealing) on the synthetic stereo pair illustrated in row 3 in Fig. 5. Column 1: disparity estimated from the canonical model, Column 2: ground truth disparity, and Column 3: disparity estimated from the proposed model. Three different regions outlined in red in rows 1, 3, and 5 are shown up close in rows 2, 4, and 6 to illustrate examples of regions were the disparity estimates produced by the canonical model were incorrect.

to 1.5 pixels. The 2D edge index was computed over 5 scales at each hierarchical scale of optimization, where the lowest scale was 1.5 pixels, and each subsequent coarser scale was larger than the previous finer scale by a factor of $\sqrt{2}$.

A linear annealing schedule comprised of 200 iterations was employed with a start temperature of 10.0 and end temperature of 0.01 for both the proposed and canonical stereo models. The temperature decrement ΔT (see Algorithm 1) was set to 0.05, while the integer disparity range ($[D_L, D_U]$ in Algorithm 1) was set to $[1, 21]$ pixels. The initial disparity estimate at the coarsest scale was set to 1 pixel everywhere.

C. Performance Measure

The stereo models were evaluated using the percent bad pixel error measure $B = \frac{1}{P} \sum_{(x,y)} (|D(x,y) - GT(x,y)| > \delta_D)$, where D is the estimated disparity, GT is the ground truth disparity, P is the total number of pixels in the image, and δ_D is the disparity error tolerance. We set $\delta_D = 1$ pixel. We report the following percent bad pixel error measures: a) percent bad

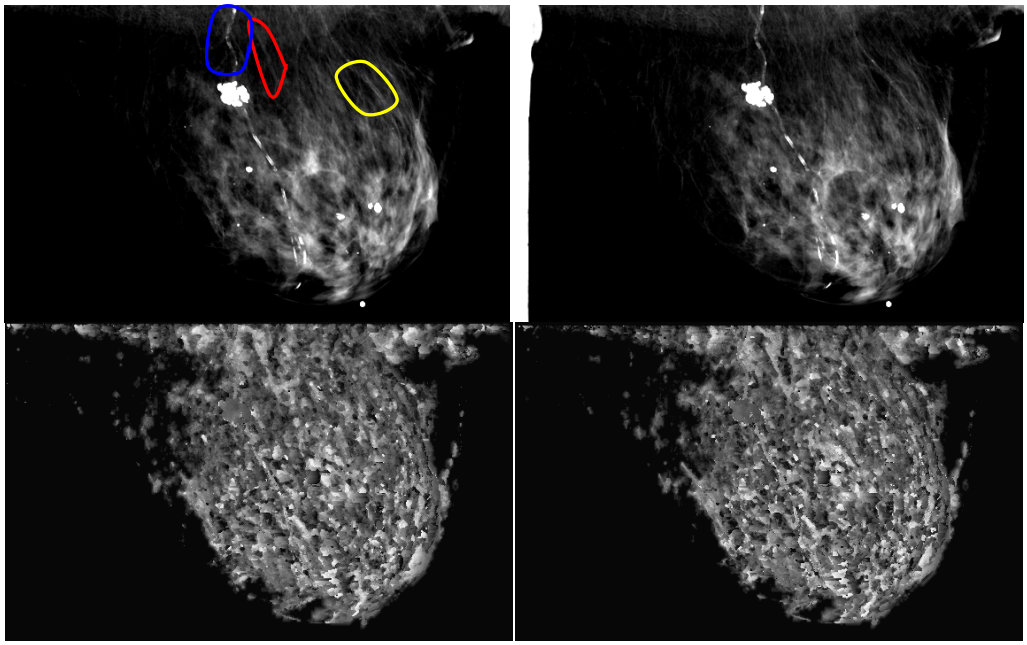

Fig. 15. An example of a real stereo mammogram image (courtesy Emory University, Atlanta, GA) and computed disparity maps. Row 1: the stereo mammogram pair with the reference image shown in the left column. The disparity in the regions outlined in color are shown up-close in Fig. 17. Row 2: computed disparity maps using the canonical stereo model (left) and the proposed stereo model (right).

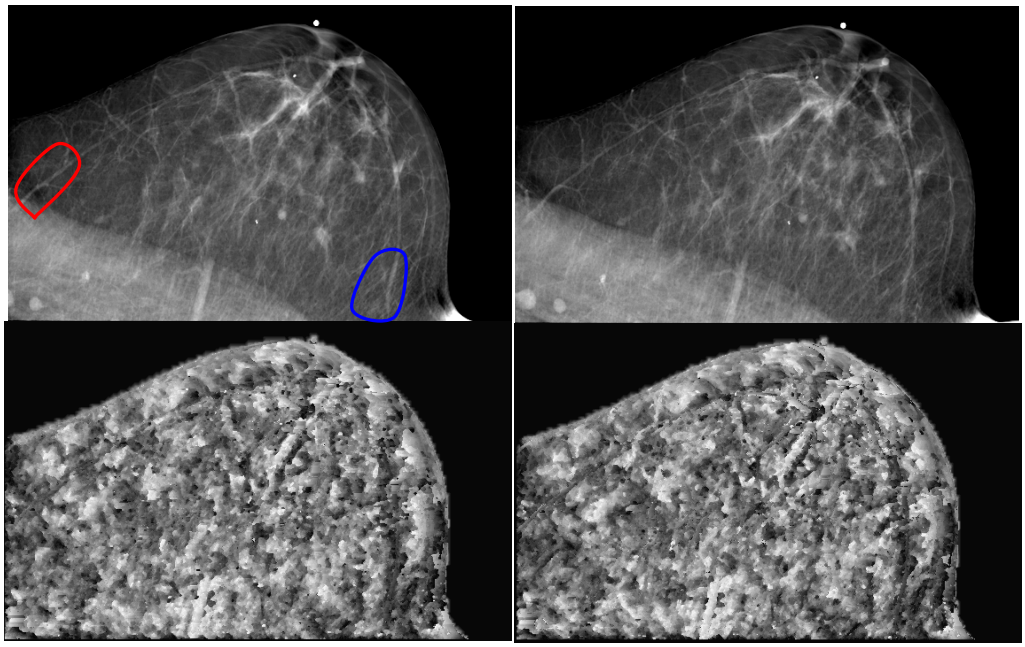

Fig. 16. Another example of a real stereo mammogram image (courtesy Emory University, Atlanta, GA) and computed disparity maps. Row 1: the stereo mammogram pair with the reference image shown in the left column. The disparity in the regions outlined in color are shown up-close in Fig. 18. Row 2: computed disparity maps using the canonical stereo model (left) and the proposed stereo model (right).

pixel error measure along curvilinear structures (B_c), b) overall percent bad pixel error measure (B), c) percent bad pixel error measure evaluated only for the non-occluded curvilinear pixels (B_{cnocc}), and d) overall percent bad pixel error measure evaluated only for non-occluded pixels (B_{nocc}). Note that B_{cnocc} and B_{nocc} were computed using the occlusion maps created from the ground truth disparity data. The difference in the performance measures of the canonical and proposed models were evaluated for statistical significance using the Wilcoxon Sign Rank (WSR) test [34].

D. Real Mammograms

The proposed and the canonical stereo models were also run on a set of five real stereo mammogram images

(courtesy Emory University, Atlanta, GA, see Figs. 15 and 16). To supplement this set, we also ran the models on a set of 48 stereo pairs created from craniocaudal tomosynthesis projection images described in detail here [7]. The two images of the stereo mammogram pair were separated by an angular spacing of 10 degrees, while the angular separation was 8 degrees for the stereo tomosynthesis pairs. Each image in both modalities had a resolution of approximately 100 microns per pixel. For computational efficiency, the images were subsampled by a factor of 4 prior to running both the stereo models. The algorithm settings used for the real stereo mammogram images were identical to the synthetic stereo images, except the disparity range was set to [1, 35] pixels. This range was arrived at by manually inspecting many landmark points that were visible on both the images of the stereo mammogram pairs.

VI. Results

Fig. 6 plots B_c computed for the proposed and the canonical stereo models for the 50 synthetic stereo images. As can be seen from Fig. 6, the proposed model clearly outperforms the single-scale and multi-scale canonical models in estimating disparity along the curvilinear structures irrespective of the optimization strategy used to optimize the canonical model (simulated annealing or graph cuts [18]. The difference in performance is statistically significant as evaluated via the WSR test ($p\text{-}value < 0.0001$ for both the single-scale and multi-scale canonical models). Also, the performance of the multi-scale canonical model is better than the single-scale model. Fig. 7 plots B computed for the proposed and the canonical stereo models for the 50 synthetic stereo images. Again, the proposed model performs better than the single-scale and multi-scale canonical models. The difference in performance is again statistically significant (WSR $p\text{-}value < 0.001$ for both the canonical models). Figs. 8 and 9 plot B_{cnocc} and B_{nocc}, respectively. The better performance of the proposed model is evident from these figures. Again, the difference in performance is statistically significant.

Figs. 10 and 11 plot B_{cnocc} and B_{nocc}, respectively for the proposed and the second order smoothness prior stereo model described in [26]. As can be seen from these figures, the proposed model clearly outperforms the second order smoothness prior stereo model on the 50 synthetic stereo images. The difference in performance is statistically significant. These results suggest that even though the model incorporates second order smoothness priors to encourage structures with curvature, which are disabled at edge locations, it does not quite promote curvilinear masses in the disparity space.

Figs. 12, 13, and 14 show the ground truth disparity (column 2), the estimated disparity maps from the multi-scale canonical model optimized using simulated annealing (column 1), and the proposed model (column 3) for the 3 synthetic stereo images illustrated in Fig. 5. The disparity maps shown in Figs. 12, 13, and 14 are pre-multiplied by the ground truth occlusion maps (see Fig. 5). Hence, occluded pixels have 0 intensity (black) in the disparity maps

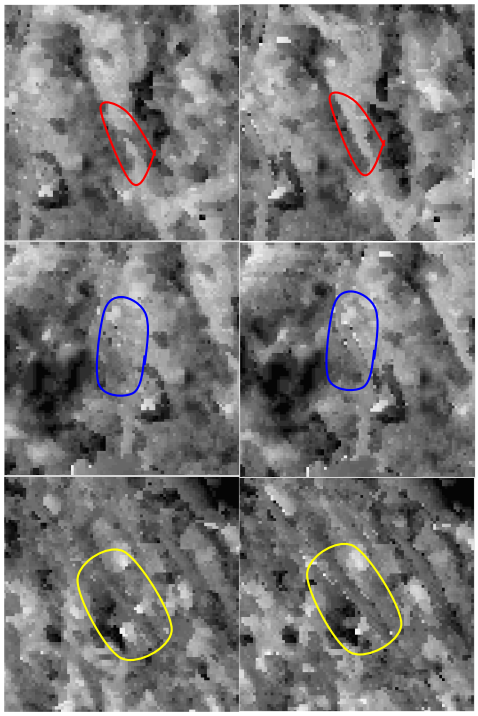

Fig. 17. Close up of the estimated disparity maps with the canonical stereo model in the left column and the corresponding region from the proposed stereo model in the right column. The color outlines correspond to the outlines in Fig. 15 and indicate regions of blurring and poor discontinuity in the disparity map produced by the canonical model.

in Figs. 12, 13, and 14. The regions outlined in red on the three disparity maps are shown up close and they illustrate some of the key regions where the canonical model produces erroneous disparity estimates and the proposed model does not. The disparity along the curvilinear masses in these regions is affected by the background disparity in the canonical model resulting in blurring, while in the proposed model they are better estimated due to the de-emphasis of smoothness at impulse and edge locations and explicit promotion of curvilinear masses in the disparity space. The results on all 50 images is made available on http://live.ece.utexas.edu/research/stereomammo/AdditionalImagesAndResults.tar.gz.

Figs. 15 and 16 shows the disparity maps estimated by the proposed and the canonical stereo models for the two real stereo mammogram images (top row). In order to visualize the results of the two models better, Figs. 17 and 18 show the close up of representative disparity regions comprising curvilinear structures (corresponding to the regions outlined in color on the reference images in Figs. 15 and 16). Figs. 17 and 18 reveal blurring and greater discontinuity in the disparity along the curvilinear structures in the estimates produced by the canonical model (left column) when compared to the proposed model (right column). While it is hard to ascertain these results quantitatively due to lack of ground truth disparity data, the proposed stereo model can be observed to preserve the curvilinear masses in the disparity space better than the canonical stereo model. The results on the entire data set is made available on http://live.ece.utexas.edu/research/stereomammo/AdditionalImagesAndResults.tar.gz. Finally, we also ran the

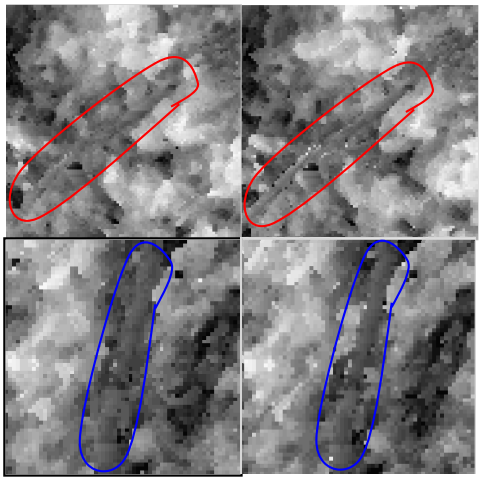

Fig. 18. Close up of the estimated disparity maps with the canonical stereo model in the left column and the corresponding region from the proposed stereo model in the right column. The color outlines correspond to the outlines in Fig. 16 and indicate regions of blurring and poor discontinuity in the disparity map produced by the canonical model.

Fig. 19. Performance of the proposed stereo model on Middlebury stereo pairs. First row: Tsukuba ($B = 0.31$), Second row: Venus ($B = 0.35$), Third row: Cones ($B = 0.39$), Fourth row: Teddy ($B = 0.40$). Column 1: left image, column 2: ground truth disparity, column 3: estimated disparity.

proposed stereo model on the standard evaluation stereo pairs (Tsukuba, Venus, Cones, and Teddy) downloaded from the Middlebury website [21] as illustrated in Fig. 19. While not explicitly designed for the Middlebury stereo pairs, the proposed model performs reasonably as is evident in Fig. 19.

VII. Conclusion

We have created a new stereo correspondence model for estimating disparity for a given pair of stereo mammogram images. The algorithm employs a recently developed singularity index [12], [13] to reliably detect locations of impulse and edge singularities in the reference image of the stereo pair. The singularity index is used to de-emphasize smoothness and promote curvilinear structures in the disparity space. Extensive experimental results on synthetic and real data show that the proposed model works. Key areas for future work include modeling the vergent geometry of the stereo mammographic image acquisition system explicitly in the computational stereo model rather than assuming that the corresponding image rows are registered, explicitly handling occlusion in the stereo model, and reconstructing 3D surfaces from the estimated disparity. Also, we plan to explore better and faster optimization algorithms such as those based on graph cuts for optimizing the proposed model [18]. There has been recent work on optimizing energy functionals containing higher order priors using graph cuts based techniques [26] and it would be interesting to explore these in the context of the proposed model. Finally, we would like to compare the proposed model with other state-of-art stereo algorithms such as those listed on the Middlebury evaluation website [21], none of which, however account for curvilinear mass structures. Unfortunately, none of the top 10 algorithms have code publicly available nor are any of the authors positively responsive to our requests.

Acknowledgment

The authors would like to thank Dr. David Getty and the Emory University at Atlanta, GA, for making available to us a set of sample stereo mammogram images.

References

[1] N. Karssemeijer *et al.*, "Breast cancer screening results 5 years after introduction of digital mammography in a population-based screening program," *Radiology*, vol. 253, no. 2, pp. 353–358, 2009.

[2] P. Skaane, "Studies comparing screen-film mammography and full-field digital mammography in breast cancer screening: Updated review," *Acta Radiol.*, vol. 50, no. 1, pp. 3–14, 2009.

[3] J. T. Dobbins, III, and D. J. Godfrey, "Digital X-ray tomosynthesis: Current state of the art and clinical potential," *Phys. Med. Biol.*, vol. 48, no. 19, pp. R65–R106, 2003.

[4] D. J. Getty, C. J. D'Orsi, and R. M. Pickett, "Stereoscopic digital mammography: Improved accuracy of lesion detection in breast cancer screening," in *Proc. 9th Int. Workshop Digit. Mammogr. (IWDM)*, 2008, pp. 74–79.

[5] J. M. Boone, A. L. C. Kwan, K. Yang, G. W. Burkett, K. K. Lindfors, and T. R. Nelson, "Computed tomography for imaging the breast," *J. Mammary Gland Biol. Neoplasia*, vol. 11, no. 2, pp. 103–111, 2006.

[6] G. S. Muralidhar *et al.*, "Stereoscopic versus monoscopic detection of masses on breast tomosynthesis projection images," *Proc. SPIE, Med. Imag., Image Perception, Observer Perform., Technol. Assessment*, vol. 8318, pp. 07-1–07-7, Feb. 2012.

[7] G. S. Muralidhar *et al.*, "Stereoscopic interpretation of low-dose breast tomosynthesis projection images," *J. Digit. Imag.*, vol. 27, no. 2, pp. 248–254, 2014.

[8] L. J. Webb *et al.*, "Comparative performance of multiview stereoscopic and mammographic display modalities for breast lesion detection," *Med. Phys.*, vol. 38, no. 4, pp. 1972–1980, 2011.

[9] C. J. D'Orsi *et al.*, "Stereoscopic digital mammography: Improved specificity and reduced rate of recall in a prospective clinical trial," *Radiology*, vol. 266, no. 1, pp. 81–88, 2013.

[10] R. Zwiggelaar, S. M. Astley, C. R. M. Boggis, and C. J. Taylor, "Linear structures in mammographic images: Detection and classification," *IEEE Trans. Med. Imag.*, vol. 23, no. 9, pp. 1077–1086, Sep. 2004.

[11] G. S. Muralidhar *et al.*, "Snakules: A model-based active contour algorithm for the annotation of spicules on mammography," *IEEE Trans. Med. Imag.*, vol. 29, no. 10, pp. 1768–1780, Oct. 2010.

[12] G. S. Muralidhar, A. C. Bovik, and M. K. Markey, "A new singularity index," in *Proc. 19th IEEE Int. Conf. Image Process.*, Sep./Oct. 2012, pp. 1873–1876.

[13] G. S. Muralidhar, A. C. Bovik, and M. K. Markey, "A steerable, multiscale singularity index," *IEEE Signal Process. Lett.*, vol. 20, no. 1, pp. 7–10, Jan. 2013.

[14] D. Scharstein and R. Szeliski, "A taxonomy and evaluation of dense two-frame stereo correspondence algorithms," *Int. J. Comput. Vis.*, vol. 47, nos. 1–3, pp. 7–42, 2002.

[15] M. Z. Brown, D. Burschka, and G. D. Hager, "Advances in computational stereo," *IEEE Trans. Pattern Anal. Mach. Intell.*, vol. 25, no. 8, pp. 993–1008, Aug. 2003.

[16] H. Hirschmuller and D. Scharstein, "Evaluation of stereo matching costs on images with radiometric differences," *IEEE Trans. Pattern Anal. Mach. Intell.*, vol. 31, no. 9, pp. 1582–1599, Sep. 2009.

[17] S. T. Barnard, "Stochastic stereo matching over scale," *Int. J. Comput. Vis.*, vol. 3, no. 1, pp. 17–32, 1989.

[18] Y. Boykov, O. Veksler, and R. Zabih, "Fast approximate energy minimization via graph cuts," *IEEE Trans. Pattern Anal. Mach. Intell.*, vol. 23, no. 11, pp. 1222–1239, Nov. 2001.

[19] R. Ben-Ari and N. Sochen, "Stereo matching with Mumford–Shah regularization and occlusion handling," *IEEE Trans. Pattern Anal. Mach. Intell.*, vol. 32, no. 11, pp. 2071–2084, Nov. 2010.

[20] E. H. Adelson, C. H. Anderson, J. R. Bergen, P. J. Burt, and J. M. Ogden, "Pyramid methods in image processing," *RCA Eng.*, vol. 29, no. 6, pp. 33–41, 1984.

[21] *Middlebury Stereo*. [Online]. Available: http://vision.middlebury.edu/stereo/, accessed May 10, 2015.

[22] N. H. Kim, A. C. Bovik, and S. J. Aggarwal, "Shape description of biological objects via stereo light microscopy," *IEEE Trans. Syst., Man, Cybern.*, vol. 20, no. 2, pp. 475–489, Mar./Apr. 1990.

[23] D. M. Chelberg, J. Hsu, C. F. Babbs, Z. Pizlo, and E. J. Delp, "Digital stereomammography," in *Proc. 2nd Int. Workshop Digit. Mammogr.*, 1994, pp. 1–10.

[24] A. Tiedeu, C. Daul, P. Graebling, and D. Wolf, "Correspondences between microcalcification projections on two mammographic views acquired with digital systems," *Comput. Med. Imag. Graph.*, vol. 29, no. 7, pp. 543–553, 2005.

[25] C.-R. Huang, P.-C. Chung, T.-Y. Lee, S.-C. Yang, and S.-K. Lee, "Reconstruction and rendering of microcalcifications from two mammogram views by modified projective grid space (MPGS)," *Comput. Med. Imag. Graph.*, vol. 30, no. 2, pp. 123–133, 2006.

[26] O. Woodford, P. Torr, I. Reid, and A. Fitzgibbon, "Global stereo reconstruction under second-order smoothness priors," *IEEE Trans. Pattern Anal. Mach. Intell.*, vol. 31, no. 12, pp. 2115–2128, Dec. 2009.

[27] J. Canny, "A computational approach to edge detection," *IEEE Trans. Pattern Anal. Mach. Intell.*, vol. PAMI-8, no. 6, pp. 679–698, Nov. 1986.

[28] W. T. Freeman and E. H. Adelson, "The design and use of steerable filters," *IEEE Trans. Pattern Anal. Mach. Intell.*, vol. 13, no. 9, pp. 891–906, Sep. 1991.

[29] G. S. Muralidhar, A. C. Bovik, and M. K. Markey, "Noise analysis of a new singularity index," *IEEE Trans. Signal Process.*, vol. 61, no. 24, pp. 6150–6163, Dec. 2013.

[30] N. H. Kim and A. C. Bovik, "A contour-based stereo matching algorithm using disparity continuity," *Pattern Recognit.*, vol. 21, no. 5, pp. 505–514, 1988.

[31] A. E. Burgess, F. L. Jacobson, and P. F. Judy, "Human observer detection experiments with mammograms and power-law noise," *Med. Phys.*, vol. 28, no. 4, pp. 419–437, 2002.

[32] J. E. Bresenham, "Algorithm for computer control of a digital plotter," *IBM Syst. J.*, vol. 4, no. 1, pp. 25–30, 1965.

[33] H. Larochelle, D. Erhan, A. Courville, J. Bergstra, and Y. Bengio, "An empirical evaluation of deep architectures on problems with many factors of variation," in *Proc. 24th Int. Conf. Mach. Learn. (ICML)*, 2007, pp. 473–480.

[34] B. Rosner, *Fundamentals of Biostatistics*, 6th ed. Belmont, CA, USA: Duxbury Press, 2005.

Gautam S. Muralidhar received the B.E. degree in electronics and communications engineering from Visveswaraya Technological University, Belgaum, India, in 2002, and the M.S.E. and Ph.D. degrees in biomedical engineering from The University of Texas at Austin (UT-Austin), in 2009 and 2012, respectively. He was a Software Engineer with Philips Healthcare, a division of Philips Electronics India Ltd., Bangalore, India, from 2003 to 2007, and the Oracle India Development Center, Hyderabad, India, from 2002 to 2003. At UT-Austin, he was a member of the Laboratory for Image and Video Engineering and the Biomedical Informatics Laboratory.

Dr. Muralidhar was a recipient of the University of Texas Continuing Graduate Fellowship from 2011 to 2012, the Medical Image Perception Society's Student Scholarship in 2011, and the University of Texas Professional Development Award in 2011.

Alan C. Bovik (S'80–M'81–SM'89–F'96) is the Curry/Cullen Trust Endowed Chair Professor with The University of Texas at Austin, where he is the Director of the Laboratory for Image and Video Engineering. He is a Faculty Member with the Department of Electrical and Computer Engineering and the Center for Perceptual Systems, Institute for Neuroscience. He has authored over 650 technical articles in his research areas, and holds two U.S. patents. His several books include the recent companion volumes *The Essential Guides to Image and Video Processing* (Academic Press, 2009). His research interests include image and video processing, computational vision, and visual perception.

He is a fellow of the Optical Society of America, the Society of Photo-Optical and Instrumentation Engineers, and the American Institute of Medical and Biomedical Engineering. He was named Honorary Member of IS&T in 2013, and received the SPIE Technology Achievement Award in 2012. He was also named the SPIE/IS&T Imaging Scientist of the Year in 2011. He received a number of major awards from the IEEE Signal Processing Society, including the best paper award (2009), the Education Award (2007), the Technical Achievement Award (2005), and the Meritorious Service Award (1998). He also received the Hocott Award for Distinguished Engineering Research at The University of Texas at Austin, the Distinguished Alumni Award from the University of Illinois at Champaign–Urbana (2008), the IEEE Third Millennium Medal (2000), and two journal paper awards from the International Pattern Recognition Society (1988 and 1993). He has been involved in numerous professional society activities, including the Board of Governors of the IEEE Signal Processing Society from 1996 to 1998, the Co-Founder and Editor-in-Chief of the IEEE TRANSACTIONS ON IMAGE PROCESSING from 1996 to 2002, an Editorial Board of the PROCEEDINGS OF THE IEEE from 1998 to 2004, a Series Editor of *Image, Video, and Multimedia Processing* (Morgan and Claypool Publishing Company, 2003-present), and a Founding General Chairman of the First IEEE International Conference on Image Processing in Austin, TX, in 1994.

Dr. Bovik is a Registered Professional Engineer in the state of Texas and a Frequent Consultant to legal, industrial, and academic institutions.

Mia K. Markey received the B.S. degree in computational biology from Carnegie Mellon University, in 1998, and the Ph.D. degree in biomedical engineering from Duke University, in 2002, along with a certificate in bioinformatics. She is an Engineering Foundation Endowed Faculty Fellow in Engineering with The University of Texas at Austin, an Associate Professor of Biomedical Engineering with The University of Texas at Austin, and an Adjunct Associate Professor of Imaging Physics with The University of Texas MD Anderson Cancer Center. Her laboratory designs decision support systems for clinical decision making and scientific discovery using artificial intelligence and signal processing technologies. Her research portfolio also includes projects in biometrics. She has been recognized for excellence in research and teaching with awards from organizations, such as the American Medical Informatics Association, the American Society for Engineering Education, and the American Cancer Society.